Volume 61
Number 66
25 August 2025
Pages 12221–12406

ChemComm

Chemical Communications

rsc.li/chemcomm

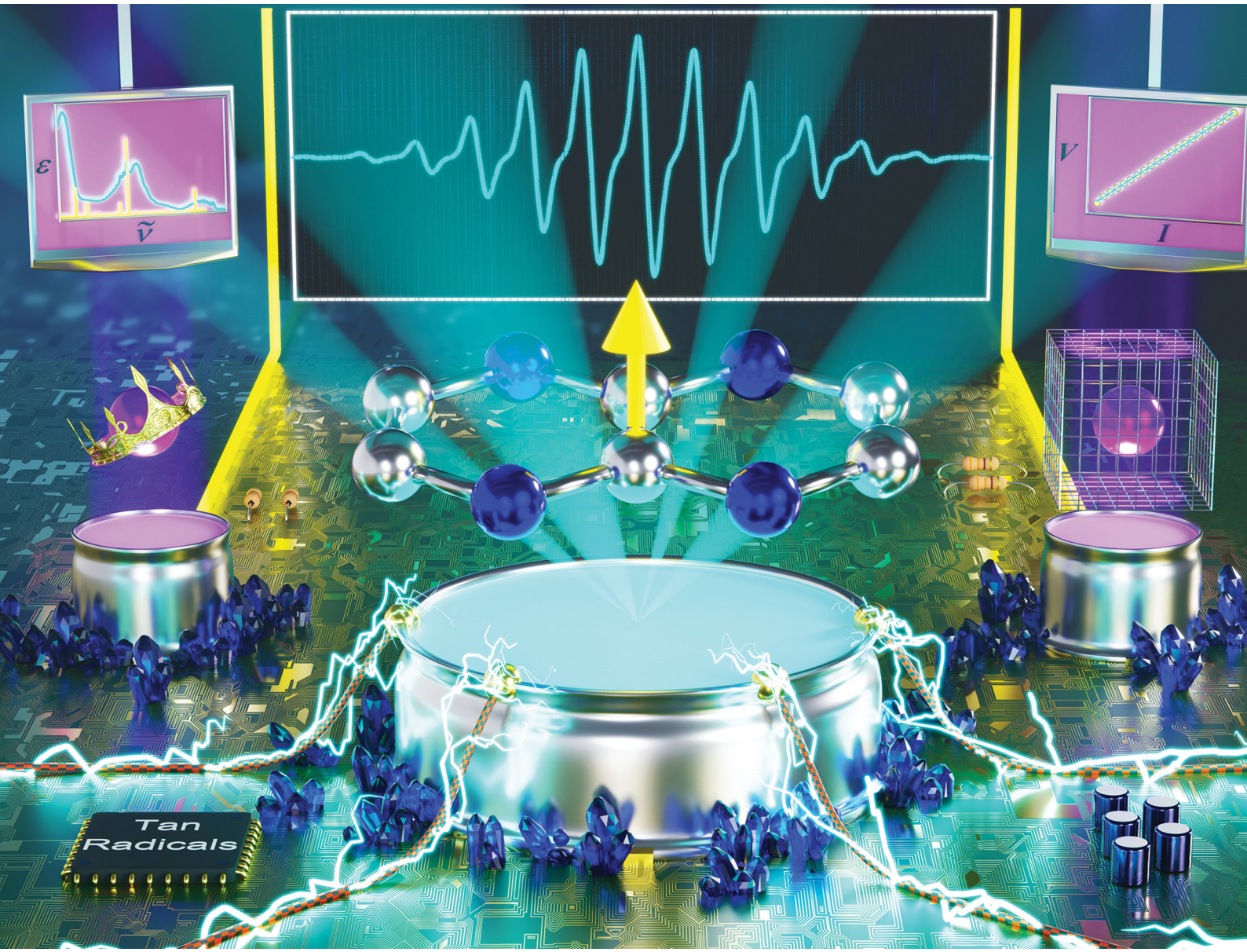

ISSN 1359-7345

ROYAL SOCIETY OF CHEMISTRY

COMMUNICATION

Saroshan Deshapriya and Selvan Demir

Isolation of 1,4,5,8-tetraazanaphthalene radicals

ChemComm

COMMUNICATION

View Article Online
View Journal | View Issue

Cite this: *Chem. Commun.*, 2025, **61**, 12301

Received 31st May 2025,
Accepted 10th July 2025

DOI: 10.1039/d5cc03096j

rsc.li/chemcomm

Isolation of 1,4,5,8-tetraazanaphthalene radicals†

Saroshan Deshapriya and Selvan Demir *

The first radicals of 1,4,5,8-tetraazanaphthalene have been synthesised and proven by crystallography, EPR spectroscopy and DFT calculations. As confirmed by four-probe conductivity measurements, the radicals are semiconducting.

The scope of organic radicals has shifted from being mere synthetic interest to functional components of advanced materials. Initially considered reaction intermediates, organic radicals are recognized as a broad class of isolable compounds with unique physical properties arising from their open-shell electronic configurations.[1,2] The inclusion of heteroatoms into conjugated π systems often leads to stable radicals owing to the delocalised unpaired spin and a lowering of the energy of the singly occupied molecular orbital (SOMO). Indeed, heterocyclic radical groups such as verdazyls, dithiazolyls, and triazinyls show ambient stability.[3] Such low-cost spin-bearing compounds are attractive for both 'green' electronics[4] and for conductive materials due to their notable electrical conductivity.[5]

Of interest are tetraazanaphthalenes innate to two fused arene rings involving four N atoms where their position can vary.[6] The redox properties of such compounds including *in situ* studies on paramagnetic states are reported;[7,8] however, isolable tetraazanaphthalene radicals with unambiguous structural characterisation are unknown to date.

Here, we report the first isolable radicals of 1,4,5,8-tetraazanaphthalene (tan), differing in the type of countercations, obtained through chemical reduction of tan. The new radicals were analysed through single-crystal X-ray diffraction (SCXRD), spectroscopy, and cyclic voltammetry. DFT computations revealed their electronic structure, while resistance measurements unveiled the radicals to be electrically conductive, placing them among semiconductors.

Department of Chemistry, Michigan State University, 578 South Shaw Lane, East Lansing, Michigan 48824, USA. E-mail: sdemir@chemistry.msu.edu

† Electronic supplementary information (ESI) available. CCDC 2455488, 2455489 and 2455490. For ESI and crystallographic data in CIF or other electronic format see DOI: https://doi.org/10.1039/d5cc03096j

Tan, **1**, was synthesized following a modified procedure,[9] and fully analysed, including an experimentally determined crystal structure.[10] Room temperature chemical reductions of tan, **1**, using potassium graphite, KC_8, in the presence of 18-crown-6 in THF and 222-cryptand in DME, afforded the radical compounds [K(18-c-6)]tan$^{\bullet}$, **2**, and [K(crypt-222)]tan$^{\bullet}$, **3**, respectively, Fig. 1. Dark-blue, needle-shaped crystals suitable for SCXRD were obtained from concentrated solutions at −35 °C overnight. **2** and **3** constitute the first crystallographically characterised radical structures of tan. Both are bottleable and stable for weeks under an argon atmosphere.

Compound **1** crystallises in the $P2_1/c$ monoclinic space group with a one body-centred molecule and four edge-centred molecules in the unit cell (Fig. S2 and S3, ESI†). The molecules are packed in layers along the crystallographic *c* axis. The experimentally observed unit cell parameters of **1** agree with those of the predicted crystal structure of tan.[10]

Compound **2** crystallises in the $P\bar{1}$ triclinic space group with half of tan$^{-\bullet}$ and half of K(18-c-6) in the asymmetric unit. An inversion centre runs through the K^+ ion bisecting the tan$^{-\bullet}$ and the countercation. The structure extends along an axis, disparate from the crystallographic axes, to a chain composed of alternating tan$^{-\bullet}$ and [K(18-c-6)]$^+$ units. The N atoms at the 1 and 5 positions are interacting with the K^+ ions of [K(18-c-6)]$^+$ leading to a one-dimensional structure, Fig. S6 (ESI†). The N···K distance of 2.869(1) Å is a stronger electrostatic interaction than the respective distances for ionic interactions in organic salts.[11,12] Furthermore, the tan$^{-\bullet}$ is planar with an average C–N bond distance of 1.352(2) Å and is slightly longer than the 1.337(1) Å of $C^{(sp2)}$–N bonds found in neutral tan, **1**, where the discrepancy is ascribed to the presence of negative charge on the compound. The central C–C bond of 1.454(2) Å is elongated by 0.039 Å relative to the corresponding bond of 1.415(1) Å in **1**, which also stems from the negative charge on tan$^{-\bullet}$.

Compound **3** also crystallises in the triclinic space group $P\bar{1}$. The asymmetric unit comprises a [K(crypt-222)]$^+$ counterion and two half-fragments of tan$^{-\bullet}$. There are two co-crystallised

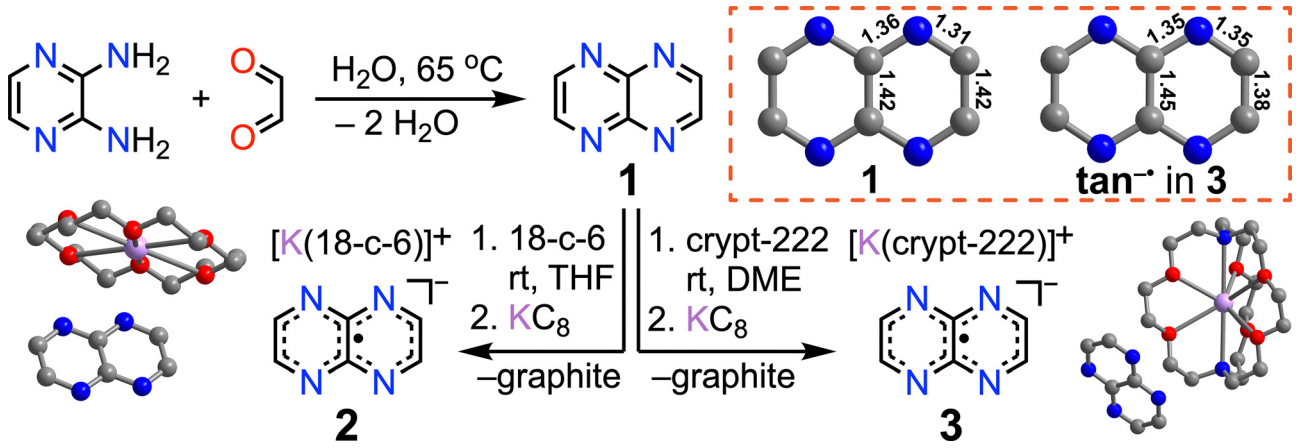

Fig. 1 Synthesis of tan, **1**, [K(18-c-6)]tan•, **2**, and [K(crypt-222)]tan•, **3**, along molecular structures of **2** (bottom left) and **3** (bottom right). Box with the dashed outline shows the molecular structures of neutral tan, **1**, and $tan^{-\bullet}$ in **3**. Distances (Å) are rounded up for clarity and full values can be found in the main text; both are planar, see Fig. S12 (ESI†). For all crystal structures: grey, blue, red and purple spheres represent C, N, O and K atoms, respectively. H atoms and co-crystallised solvent molecules have been omitted for clarity.

DME solvent molecules in **3**, disparate from the unit cell of **2**. Compound **3** features no long-range chain-like structure, and no interactions between the K^+ ion and the N atoms of $tan^{-\bullet}$ which is attributed to a fully encapsulated K^+ ion by the cryptand.

Akin to **2**, the $tan^{-\bullet}$ is fully planar in **3**. The average C–N bond distance of 1.352(2) Å and the central C–C bond of 1.448(3) Å in **3** resemble the values of **2**. Thus, the change of the countercation affords differences in intermolecular interactions and crystal packing effects but does not impact the metrical parameters of the $tan^{-\bullet}$ unit. The $tan^{-\bullet}$ radicals are compared to our reported $flv^{-\bullet}$ (fluoflavine) radical,[13] which was isolated in the form of [K(Crypt-222)]flv• and features two peripheral phenyl rings fused to the tan scaffold. The structures are topologically similar, enabling a bond metrics comparison. In $flv^{-\bullet}$ of [K(Crypt-222)]flv•, the average C–N distance is 1.352(2) Å and the central C–C distance is 1.466(3) Å, akin to those found in **2** and **3**.

Electrochemical measurements of **3** in a $[^nBu_4N][PF_6]$ electrolyte solution in 1,2-difluorobenzene exhibited two quasi-reversible redox events at −1.96 V and −1.04 V (Fig. 2A), referenced against the ferrocene redox couple, which are ascribed to the $tan^{2-}/tan^{-\bullet}$ and $tan^{-\bullet}/tan^0$ redox couples, respectively. The potentials are comparable to the redox events of −1.60 V and −0.90 V observed for the $flv^{-\bullet}$ radical anion in [K(Crypt-222)]flv•. The two redox events can be separately observed when performing isolated voltage scans, suggesting that each oxidation state can be reached independently (Fig. S28 and S29, ESI†). The electrochemical behaviour of **2** features a similar trend to that of **3** (Fig. S24–S26, ESI†).

The radical nature of **2** and **3** was proven by X-band cw-EPR spectroscopy (Fig. 2 and Fig. S22, ESI†). The EPR measurements were conducted on 0.5 mM solutions from 300 to 160 K in 20 K decrements. Since **2** and **3** exhibit similar spectra, the spectrum of **3** is discussed in the following. The cw-EPR spectrum of **3** at 300 K exhibits 11 main lines, which were simulated using a *g* value of 2.0035 and 9.29 MHz and 8.74 MHz hyperfine coupling constants for ^{14}N and ^1H nuclei, respectively. The simulation parameters are similar to cw-EPR data obtained on solutions of tan radicals, albeit never isolated or crystallographically characterised.[7,8] In addition, no change in hyperfine coupling constant occurs with varying temperature (Fig. S22, ESI†), indicating that the distribution of the unpaired electron on $tan^{-\bullet}$ shows minimal temperature dependence.

While the solid-state structure of the tan radicals is uncovered through crystallography, the solution-state is revealed through the analysis of the relative intensities of the cw-EPR spectra. A cw-EPR spectrum displays the first derivative of the signal, whereas double integration (DI) of the EPR spectrum uncovers the number of spins present in the sample. When instrument parameters are kept constant, DI of cw-EPR enables scrutiny of the solution-state behaviours of radicals.

Cw-EPR spectra of **2** and **3** were collected on THF solutions of 0.5 mM concentration, at temperatures from 300 to 160 K in 20 K decrements. For calibration of spin counting experiments, the EPR standard triacetoneamine-*N*-oxyl (TEMPONE) radical solution was used at the same concentration. The derived DI values for **2** and **3** at each temperature were divided by the corresponding DI value of TEMPONE to exclude the effects of resonator expansion, solvent viscosity changes and other external factors. When traversing from 300 to 220 K, the $DI_{tan}/DI_{TEMPONE}$ ratio gradually decreases for both **2** and **3**, Fig. 2D. This intensity loss can have two origins: either (a) owing to power saturation effects where at lower temperatures the excited spin level relative population is higher due to slow spin–lattice relaxation of the excited spins. In our case, power saturation at 160 K can be ruled out as the spectra were collected at microwave powers below saturation; or (b) π-dimerisation arising from two planar, π-conjugated radicals that come into close contact with each other, causing the EPR intensity to drop. Thus, π-dimerisation occurs in solutions of **2** and **3** and considering the change in DI with temperature, the dimers behave very similarly. As a further implication, the impact of the countercation onto the solution-state dynamics is minimal and thus, negligible. The conceivable π-dimers were modelled using DFT computations (Fig. S31, ESI†).

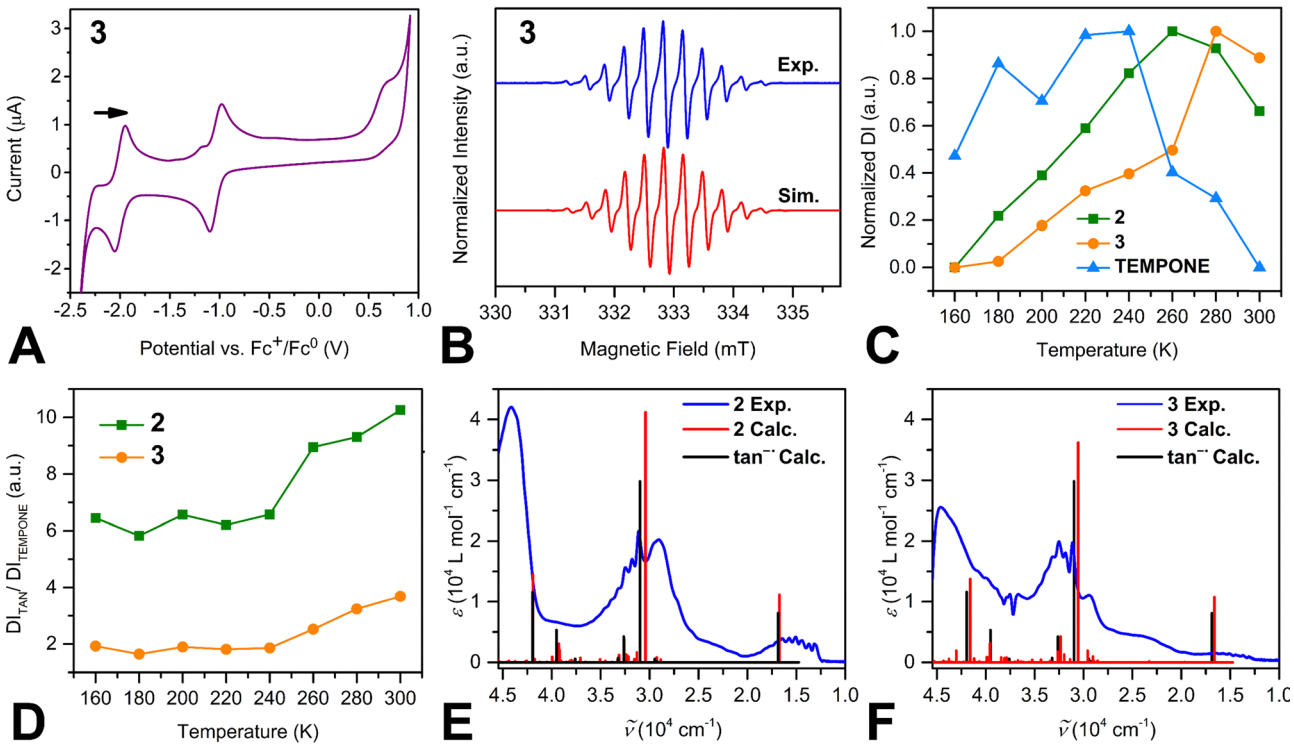

Fig. 2 (A) Cyclic voltammogram of [K(crypt-222)]tan•, **3**, *vs.* Fc. (B) X-band cw-EPR spectrum of **3**. The experimental spectrum was collected at 300 K (blue trace) and the simulation is shown in red trace. (C) Temperature dependence of normalized EPR double intensity (DI) values of **2** (green squares), **3** (orange circles), and the standard TEMPONE (light blue triangles). (D) Corrected EPR DI values of **2** (green squares) and **3** (orange circles) obtained by dividing the DI of tan$^{-\bullet}$ by DI of TEMPONE at each respective temperature. UV-Vis spectra of (E) 20 μM solution of **2** and (F) 15 μM solution of **3**. Both spectra (blue trace) were collected in THF from 220 nm to 1000 nm. The red vertical lines correspond to predicted TD-DFT transitions. Black vertical lines exhibit the predicted transitions for the tan$^{-\bullet}$ fragment.

At temperatures between 220 and 160 K, the DI value remains invariant for both **2** and **3**. This may be ascribed to the Boltzmann population effects being more significant at lower temperatures, *i.e.* the thermal population of the excited state is lessened as the temperature is reduced, and hence, the ground state spins will absorb more microwave radiation. This is reflected by a higher amplitude in the EPR spectrum, concomitant with a higher DI value. Furthermore, the cw-EPR spectra collected from 300 to 180 K do not feature broadening, indicative of the spin–spin relaxation time not substantially changing in this temperature range. A slight broadening is observed at 160 K, which is ascribed to THF being frozen below 164.8 K (Fig. S22, ESI†).

To gain insight into the electronic structure, DFT calculations were performed on both compounds where the crystal coordinates of **2** and **3** were first geometry optimised. The coordinates analysis *via* frequency calculations (Fig. S15 and S16, ESI†) exhibited no imaginary frequencies and thereby the presence of an energetically minimum structure was verified. The spin densities for **2** and **3** are identical and unaffected by the counterion, Fig. 3. The spin densities are derived from optimised crystal coordinates precluding a correlation to the EPR hyperfine assignments as the spectroscopy was carried out on solutions that may differ from the solid-state structures.

The optimised coordinates of (a) the tan$^{-\bullet}$ fragment, (b) [K(18-c-6)]tan•, **2**, and (c) [K(crypt-222)]tan•, **3**, were employed

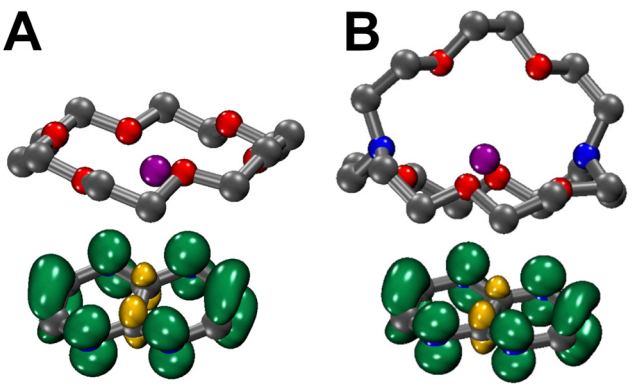

Fig. 3 Spin density distributions of (A) **2** and (B) **3**. Grey, blue, red, and purple spheres represent C, N, O and K atoms, respectively. H atoms are omitted for clarity. Green and yellow surfaces represent spin density. Isovalue for surfaces set at 0.003.

in time-dependent DFT (TD-DFT) calculations to project UV-Vis spectra, Fig. 2E and F. The major TD-DFT transitions predicted for all systems are similar, indicating the negligible effect of the counterion on the electronic absorption spectrum. A shift by 0.25 eV of the computed TD-DFT transitions increased congruence with the experimental spectra.

UV-Vis spectra were taken on a 20 μM solution of **2** and a 15 μM solution of **3** in THF. The blue solutions exhibit similar

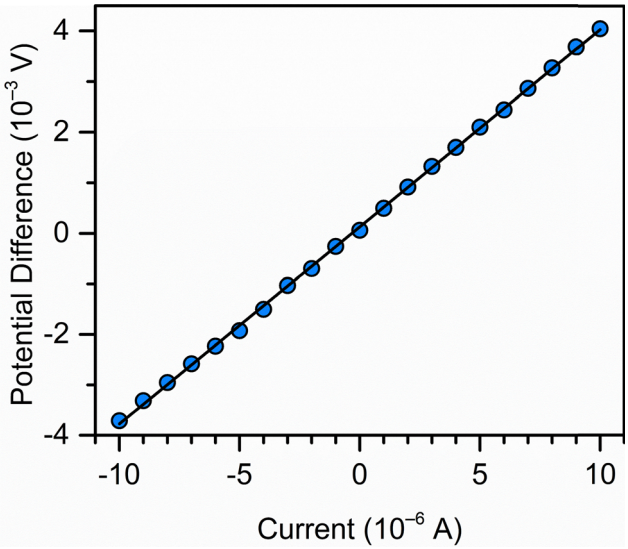

Fig. 4 Current *vs.* voltage data collected from −10 to 10 μA on a crystal of **2** at room temperature. Blue circles represent experimental data points, and the black line corresponds to the fit. Fit parameter, R^2 = 0.999.

key absorption features in the range of 220 to 1000 nm. In the visible region, the largest absorption feature is centred at 1.68 × 10^4 cm^{-1} (597 nm). This feature possesses a more apparent fine structure and arises from a SOMO to LUMO excitation. The second largest absorption peak at 3.04 × 10^4 cm^{-1} (330 nm) exhibits fine structure and stems from an excitation from HOMO−1 to the unoccupied spin manifold of SOMO. While both compounds exhibit this feature, the shoulder peak at lower frequencies in **3** (∼2.9 × 10^4 cm^{-1}, 345 nm) is less intense relative to that of **2**. The highest absorption peaks for both compounds lie in the UV region at 4.19 × 10^3 cm^{-1} (238 nm) and originate from an electronic excitation from HOMO−2 to LUMO.

π-conjugated organic radicals exhibit electrical conductivity,[5] which prompted us to pursue four-probe electrical resistance measurements on $tan^{-\bullet}$. These measurements were conducted on single crystals under the exclusion of air and moisture at room temperature (see Section S5 of the ESI†).

The current *vs.* voltage measurement produced a linear response for the crystal of **3** at all current levels. The data collected from −10 to 10 μA are shown in Fig. 4, alongside a fit to the data, generating a slope value, resistance, of 390 Ω. Similarly, through the measurements at each current value (Fig. S20, ESI†), the resistance was determined to be an average of 377 Ω. The electrical behaviour of the system remained invariant upon exposure or protection from light. The resistivity was calculated taking into account the crystal dimensions (Fig. S21, ESI†) affording an electrical conductivity of 2.43 S m^{-1}, comparable to other organic radicals such as spiro-biphenalenyl radicals,[14] and to undoped elemental germanium (∼2.2 S m^{-1}).[15] The origin of the electrical conductivity is ascribed to thermally activated electron hopping mechanisms, akin to those apparent in other organic radicals.[5] The conductivity of **2** was found to be 0.01 S m^{-1} (Fig. S18 and S19, ESI†), which is higher than that of semiconducting silicon (∼4 × 10^{-4} S m^{-1}). The reduced electrical conductivity of **2** relative to **3** is ascribed to the larger distances between $tan^{-\bullet}$ radicals in the solid state of **2** (Fig. S7, ESI†).

In conclusion, tan was first identified through SCXRD, purified, and employed in chemical reductions which led to the first isolation and characterisation of $tan^{-\bullet}$ radicals with two differing counterions, $[K(18\text{-c-}6)]^+$ and $[K(crypt\text{-}222)]^+$. EPR spectra hint at π-interactions, such as dimerisations, and show that the unpaired electron distribution is not affected by the counterion. This interpretation is supported by the DFT calculations and obtained UV-Vis spectra. Excitingly, **2** and **3** are semiconducting in the solid-state, where **3** is comparable to superior semiconductors such as elemental germanium at room temperature, highlighting the potential of utilizing $tan^{-\bullet}$ species as a molecular building block in spintronic devices and in electronic applications at large.

This work was funded in part through the National Science Foundation (NSF) Faculty Early Career Development Program (CAREER) CHE-2339595. The authors are grateful to the computational resources and services provided by the Institute for Cyber-Enabled Research. The authors gratefully acknowledge Prof. Tim Hogan (MSU) for guidance and help with resistance measurements.

Conflicts of interest

There are no conflicts to declare.

Data availability

CCDC 2455488, 2455489 and 2455490 contain the crystallographic data for this paper. The other characterization data supporting this article have been included as part of the ESI.†

Notes and references

1 Z. X. Chen, Y. Li and F. Huang, *Chem*, 2021, **7**, 288–332.
2 F. Benner, L. La Droitte, O. Cador, B. Le Guennic and S. Demir, *Chem. Sci.*, 2023, **14**, 5577–5592.
3 C. P. Constantinides and P. A. Koutentis, *Advances in Heterocyclic Chemistry*, Elsevier, 2016, vol. 119, pp. 173–207.
4 J. E. Anthony, A. Facchetti, M. Heeney, S. R. Marder and X. Zhan, *Adv. Mater.*, 2010, **22**, 3876–3892.
5 D. Yuan, W. Liu and X. Zhu, *Chem*, 2021, **7**, 333–357.
6 I. G. Cuesta, A. S. De Merás and P. Lazzeretti, *J. Comput. Chem.*, 2006, **27**, 1980–1989.
7 R. Danieli, L. Lunazzi and G. Placucci, *J. Am. Chem. Soc.*, 1971, **93**, 5850–5852.
8 G. F. Pedulli and M. Guerra, *J. Magn. Reson.*, 1978, **32**, 243–249.
9 W. L. F. Armarego, *J. Chem. Soc.*, 1963, 4304.
10 M. J. Robey, M. Sterns, H. M. Morris and I. G. Ross, *J. Cryst. Mol. Struct.*, 1971, **1**, 401–403.
11 K. F. Tesh, T. P. Hanusa and J. C. Huffman, *Inorg. Chem.*, 1990, **29**, 1584–1586.
12 A. I. Ojeda-Amador, A. J. Martínez-Martínez, G. M. Robertson, S. D. Robertson, A. R. Kennedy and C. T. O'Hara, *Dalton Trans.*, 2017, **46**, 6392–6403.
13 F. Benner and S. Demir, *J. Am. Chem. Soc.*, 2024, **146**, 26008–26023.
14 X. Chi, M. E. Itkis, K. Kirschbaum, A. A. Pinkerton, R. T. Oakley, A. W. Cordes and R. C. Haddon, *J. Am. Chem. Soc.*, 2001, **123**, 4041–4048.
15 B. S. Mitchell, *An Introduction to Materials Engineering and Science: For Chemical and Materials Engineers*, Wiley, 1st edn, 2003.

